Finite Element Analysis of the Inflatable Re-Entry Vehicle Experiment

Lin Li,[1] Keir C. Gonyea,[2] and Robert D. Braun[3]
Georgia Institute of Technology, Atlanta, GA, 30332

Hypersonic inflatable aerodynamic decelerator technology can enable future missions to Mars and the outer planets. Such missions require large drag devices to safely decelerate the vehicle during planetary entry. Key technologies include flexible materials that will protect the spacecraft from the thermal environment experienced during reentry into the atmosphere. An improved understanding and predictive capabilities of the decelerator behavior is necessary prior to flight. Accurate prediction of the decelerator structural response under various external pressure distributions is necessary through use of modeling and simulation. In order to validate the predictions obtained from finite element analysis and computational fluid dynamic analysis, a series of ground and flight tests have been conducted. Sub-scale models were used for these tests due to the cost and limitations of test facilities. This investigation models the decelerator configuration with the intent of constructing less computationally-expensive models to approximate the structural response. Modeling results are compared with similar results in the literature as well as idealized closed-form equations. These results include the meridional shell force resultants in the tori, spars, and restraint wrap fore and aft side. Due to symmetry, a three dimensional, 15° wedge model and a two dimensional, axisymmetric model are used. After the model was developed, the equilibrium deflected solution and Von Mises stresses were calculated and analyzed. These results correlated well with the closed-form equations and results from literature. This investigation demonstrates that sufficient accuracy can be obtained using two-dimensional, axisymmetric models.

[1] Graduate Research Assistant, School of Aerospace Engineering, lli313@gatech.edu, AIAA student member
[2] Graduate Research Assistant, School of Aerospace Engineering, keir@gatech.edu
[3] David and Andrew Lewis Professor of Space Technology, School of Aerospace Engineering, robert.braun@aerospace.gatech.edu, AIAA Fellow

Nomenclature

A	Vehicle reference area
α	Sphere cone angle
β	Ballistic coefficient
C_D	Drag coefficient
D_A	Aeroshell diameter
D_C	Center-body diameter
D_T	Toroid diameter
H_s	Height of spar fabric
m	Vehicle mass
m_c	Mass of center-body
N_{MAX}	Fabric running load
P	Inflation pressure
q	Aerodynamic surface pressure
W_S	Width of spar fabric spacing between tori

Acronyms

DOF	Degree Of Freedom
FEA	Finite Element Analysis
HIAD	Hypersonic Inflatable Aerodynamic Decelerator
IRVE	Inflatable Reentry Vehicle Experiment
TPS	Thermal Protect System
TRL	Technical Readiness Level

I. Introduction

Inflatable structures have many military, architectural, and aerospace applications. Recent successful implementations of inflatable aerospace structures include the airbag impact attenuation system for the Mars Exploration Rover and Orion capsule. There are also ongoing research projects involving inflatable structures for use during space missions. Examples include inflatable habitats, pressurized structures potentially capable of supporting life in outer space, or supersonic inflatable decelerators currently being developed by the Low Density Supersonic Decelerator project. Another current project is the development of the Hypersonic Inflatable Aerodynamic Decelerator (HIAD). HIADs are under consideration for use as large heat shields to protect payloads against the severe aerodynamic heating experienced while entering planetary atmospheres such as Mars or Earth.

When designing a vehicle for atmospheric entry, it is necessary to consider four critical parameters: peak heat flux, integrated heat load, peak deceleration, and peak dynamic pressure. Generally, peak heat flux and dynamic pressure determine the TPS material and the integrated heat load is used to size the TPS thickness. Peak deceleration limits the mission type since different payloads have different critical loading parameters.

The vehicle characteristic that has the largest affect on the nature of the entry profile, in terms of heating and deceleration, is the ballistic coefficient, $\beta = \frac{m}{C_D A}$. Smaller ballistic coefficients yield lower peak heat flux, integrated heat load, and peak deceleration. A lower ballistic coefficient vehicle is also able to land the same amount of mass at higher altitude or more mass at the same altitude. For a given payload it is difficult to decrease the vehicle mass. Therefore, in order to lower the ballistic coefficient, it is desired to increase the vehicle diameter without significantly increasing the mass. This is not practical with a rigid heat shield since their diameter cannot be increased beyond the diameter of the rocket payload fairing. It can, however, be resolved by employing an inflatable aeroshell since they are able to increase the drag area with a minor increase in mass.[2]

II. Objectives

The main goal of this project is to investigate the fabric stresses and deflection of a HIAD under an internal inflation and external aerodynamic load. Results will be validated by comparing with closed-form equations and results from the literature. Two different models are constructed. One is a 3D, 15° wedge and the other is a 2D, axisymmetric model. Mesh convergence analysis is performed to ensure that the mesh is sufficient to accurately resolve the results.

III. Finite Element Analysis Modeling and Results

A. Model Assumptions

The IRVE configuration is composed of a center-body structure and inflatable aeroshell, shown in Fig. 1. The center-body structure, made of aluminum, contains the electronics, inflation subsystem, and rigid nose cone. The inflatable aeroshell consists of seven tori, separated into three volumes. The three volumes are laced together and covered by a restraint wrap. The tori are made of a silicone coated Kevlar fabric while the restraint wrap is made of a layup of dry Kevlar fabric to support structural loads, Nextel 312 cloth for thermal protection, and Kapton acting as a gas barrier.[3]

The FEA model developed here does not include the center-body structure and is focused on the inflatable aeroshell. The center-body is incorporated into the model via boundary conditions. The point on the innermost tori in contact with the center-body is restrained from moving up and down and the fore and aft restrain wraps are clamped where they join the center-body. In the IRVE flight test article, the restraint wrap is attached to the tori at the outer diameter of the outermost tori and contacts, but is not attached to, the remaining tori at their tangent points. In this model, the wrap is assumed to be attached at all tangent points. In addition, all spars are modeled as a continuous fabric connecting two adjacent tori (in reality the spars within the same volume are segmented into 16 sections with half-inch wide gaps to equilibrate pressure). The aerodynamic load on the wrap is assumed to be uniform, while in reality the maximum load occurs at the fabric/center-body interface.

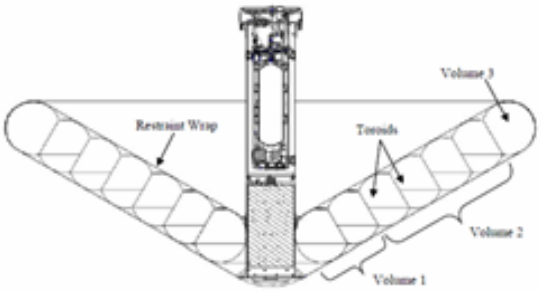

Figure 1. Cross-section of IRVE[3]

B. Material Models

FEA was performed using two different material models; an isotropic material property model and a more complex model using orthotropic material properties. The isotropic model was created to check the model, boundary conditions and loading; the orthotropic model was used to validate the results with the closed-form equations and literature values (the literature model also employed orthotropic material properties). The orthotropic properties themselves are an approximation to the nonlinear fabric properties from the flight test vehicle.

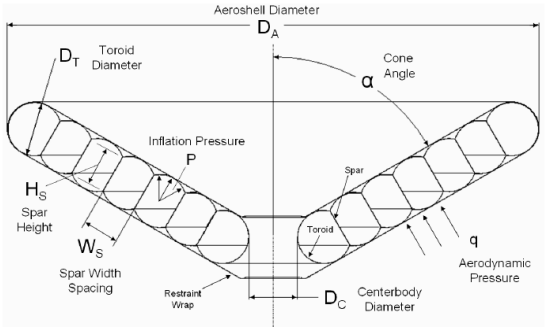

Figure 2. Sphere-cone geometry[3]

C. Model Geometry

Figure 2 shows a cross-sectional view of the rotationally symmetric IRVE geometry. The inflatable aeroshell has a cone angle (α) of 60°. The outer radius of the model (D_A) is 1.5 meters and the diameter of each individual torus (D_T) is 0.305 meters. The center-body diameter (D_C) is 0.273 meters and the spar width spacing (W_S) is 0.204 meters. Only the right side of Fig. 2 was modeled in ANSYS since it is symmetric. In the model, the geometry cross-section lies in the *xy*-plane with the origin at the intersection of the symmetry axis and a virtual extension of the forward (bottom) wrap. The tori were constructed based on their center points and radii, the spars from the tori intersections and the wrap from the tori tangent points. For the 3D wedge model, this cross section was revolved by 15° about the y-axes. The plots of wedge model cross-section and geometry are shown in Figs. 3 and 4. The thickness of the material was specified in the shell elements.

The 2D axisymmetric model was created from 2D plane elements. Therefore, the thickness was incorporated directly into the geometry. To create the tori for the axisymmetric model, two concentric circles with different radii were generated, evenly spaced around the torus radius and with a spacing of the material thickness, shown in Figs. 5 and 6. The spars and wrap were created in a similar manner. In the final solution, the tori penetrated slightly into the forward restraint wrap. Since contact modeling on these surfaces would be prohibitively expensive (19 symmetric contact sets between adjacent tori and the forward wrap), contact was instead enforced by adding a very low elastic

modulus ‘filler’ material between the gaps of the tori and forward restraint wrap, seen in Fig. 7. This filler material prevented penetration of the surfaces while minimally affecting the stiffness of the structure. In addition, due to the simplicity of the area addition and the fact that its internal stress distribution was not critical, use of this filler material resulted in a much lower increase in computational expense.

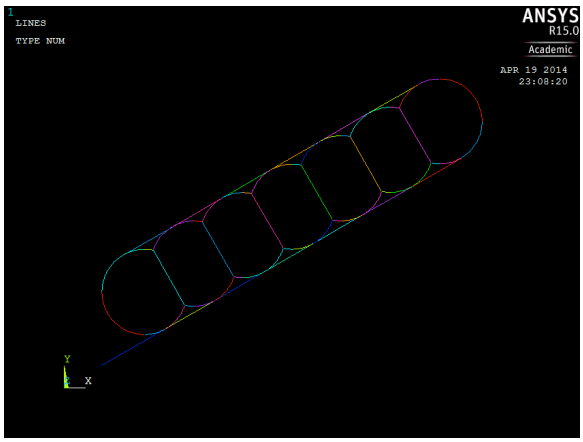

Figure 3. Cross-section of 15° wedge model

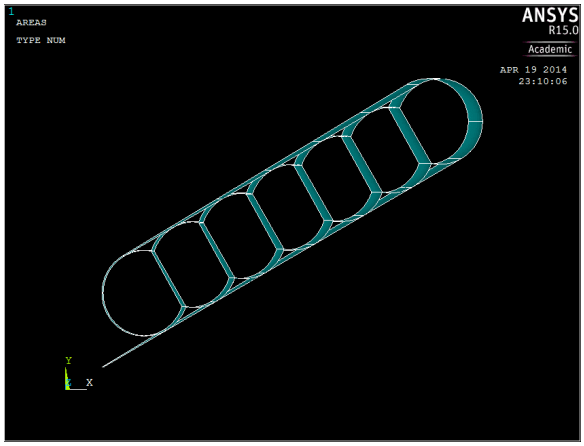

Figure 4. 15° wedge model

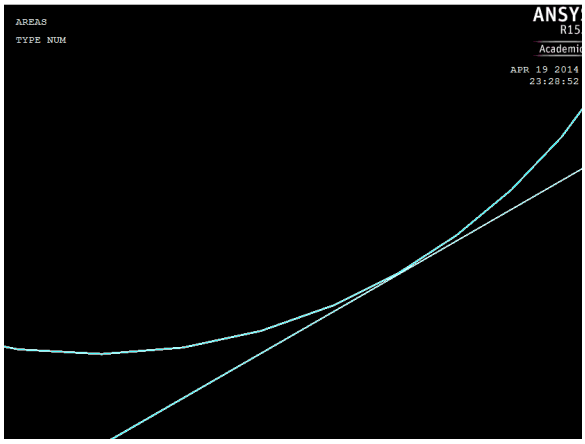

Figure 5. Tori geometry for axisymmetric model

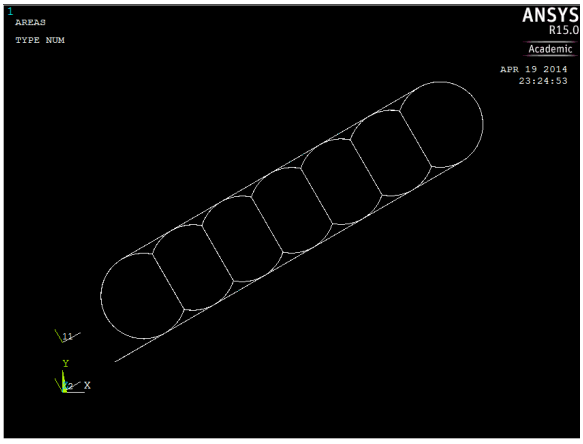

Figure 6. Axisymmetric model

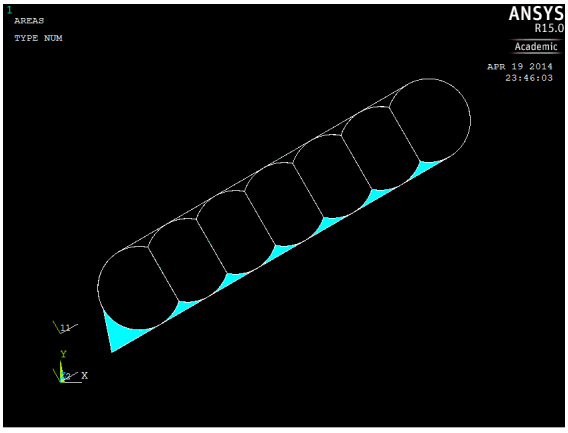

Figure 7. Model geometry with filler material

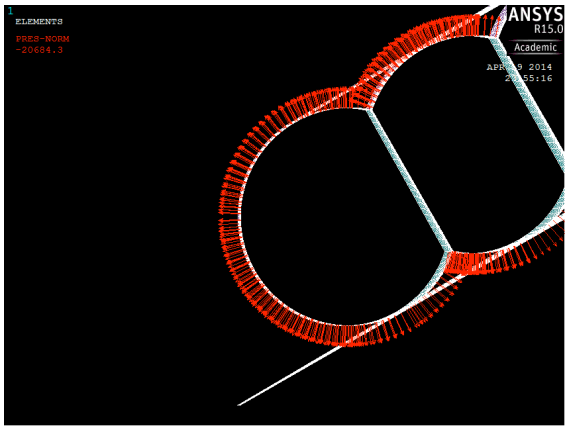

Figure 8. Applied internal inflation pressure on the inner surface of tori

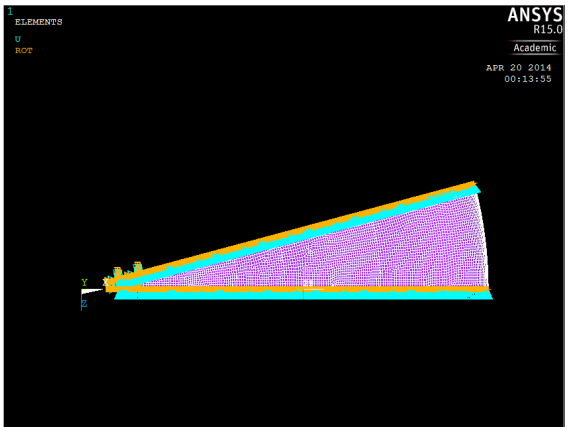

Figure 9. Symmetry boundary conditions on outermost nodes along symmetry planes

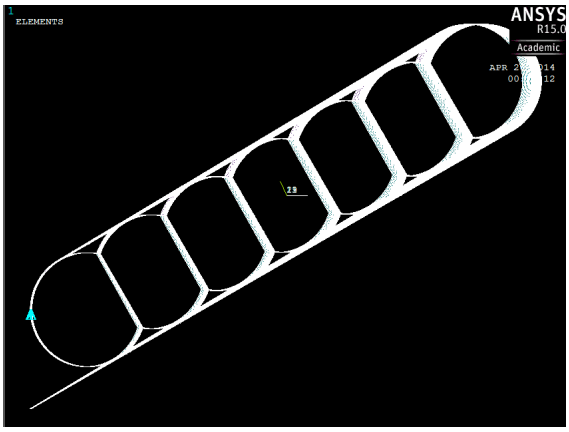

Figure 10. Roller boundary conditions on inner surface of innermost torus

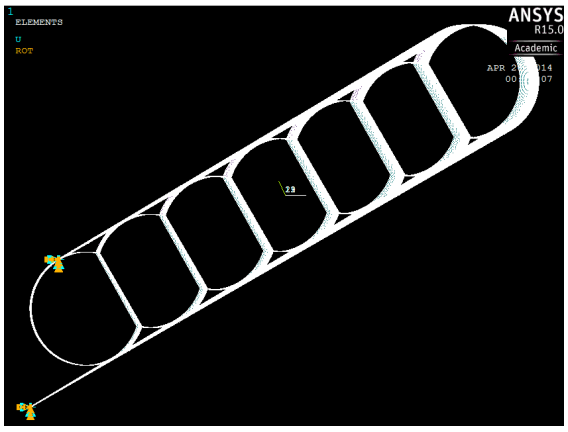

Figure 11. Clamped boundary conditions at the restraint wrap ends

D. Loading Conditions

Two different loads were applied to the model: the internal inflation pressure of the tori and the external dynamic pressure during reentry. The inflation pressure was applied to the inner surface of all tori, seen in Fig. 8. Given that all inflatable volumes had the same internal inflation pressure, there was no resultant pressure on the spars. The aerodynamic pressure was applied to the outer surface of the forward (bottom) restraint wrap. The values of the applied forces were based on a single point in the IRVE flight test trajectory and are the same values used in the literature. This corresponds to a 3.0 psi internal inflation pressure and 0.22 psi uniform aerodynamic surface pressure.

E. Boundary Conditions

Since the IRVE test article has axially symmetric geometry, material properties, boundary conditions and loading the FEA modeled employed axial symmetry to reduce computational cost. The boundary conditions for the 3D 15° wedge model are listed in Table 1. In both Tables 1 and 2, a blank entry denotes no constraint while a *'0'* entry denotes a constrained boundary condition with value of 0. Nodes along the symmetry planes are constrained from moving in the U_θ direction and from rotating about the R_R and R_Y axes, shown in Fig. 9. The points on the inner torus in contact with the center-body are constrained from translating in the U_Y direction and the ends of the forward and aft wrap closest to the center-body employ clamped boundary conditions, constraining all degrees of freedom. These can be seen in Figs. 10 and 11.

The boundary conditions for the axisymmetric model are listed in Table 2. In this model, the symmetry boundary conditions are automatically enforced. The U_Y degree of freedom is constrained for the points on the inner torus in contact with the center-body and all degrees of freedom are constrained for the end of the forward and aft wrap.

Table 1. Boundary conditions for the 15° wedge model

Symmetric Boundary Conditions						Roller Boundary Conditions						Clamped Boundary Conditions					
Translation			Rotation			Translation			Rotation			Translation			Rotation		
U_R	U_θ	U_Y	R_R	R_θ	R_Y	U_R	U_θ	U_Y	R_R	R_θ	R_Y	U_R	U_θ	U_Y	R_R	R_θ	R_Y
	0			0				0	0	0		0	0	0	0	0	0

Table 2. Boundary conditions for the axisymmetric model

Roller Boundary Condition			Clamped Boundary Condition		
Translation		Rotation	Translation		Rotation
U_X	U_Y	R_Z	U_X	U_Y	R_Z
	0		0	0	0

F. Results

A series of models were investigated to understand the tradeoff between accuracy and computational efficiency. The axisymmetric model was run with both isotopic and orthotropic material properties. The orthotropic model was solved using both a nonlinear and linear solver. The linear solution was compared to the 15° wedge model (also employing a linear solver) and the nonlinear solution was compared with the model containing the filler material.

Results of the linear analysis are shown in Figs. 12-14. The linear wedge model solution shows significant distortion of the tori and forward wrap surfaces. When focusing on the intersections of the tori, wrap and spars it is evident that there is significant penetration of the surfaces. The solution of the axisymmetric plane model looks almost identical, displaying the same warping of the tori and forward wrap but with slightly higher deflection values. It should be noted that the largest applied force in these models is the inflation pressure, acting radially outward on each torus. Therefore, these solutions are not physically representative as evidenced by the concave surfaces and significant amount of surface penetration.

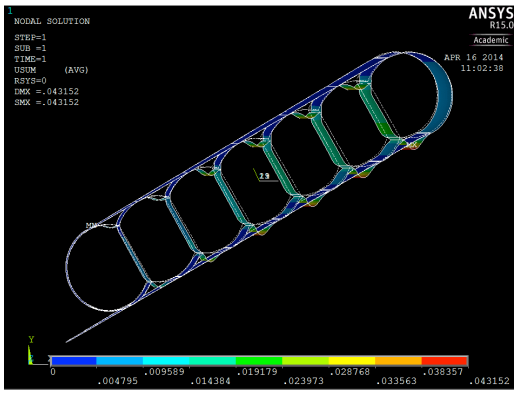

Figure 12. Linear solution for wedge model

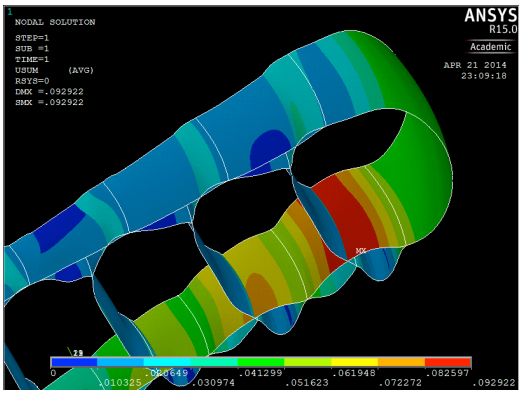

Figure 13. Wedge model surface penetration

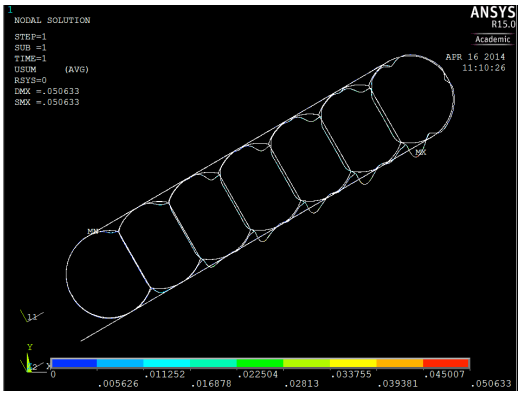

Figure 14. Linear axisymmetric model solution

Results of the nonlinear analysis are shown in Figs. 15-17. The nonlinear axisymmetric model solution has a reasonable shape with no significant warping of the surfaces. Focusing on the tori-wrap intersection area in Fig. 16, it is evident that a slight amount of surface penetration is occurring. However, compared to the model scale this penetration is very small. In Fig. 17, the filler area is added to prevent surface penetration by physically having a barrier to contact. This solution also looks reasonable.

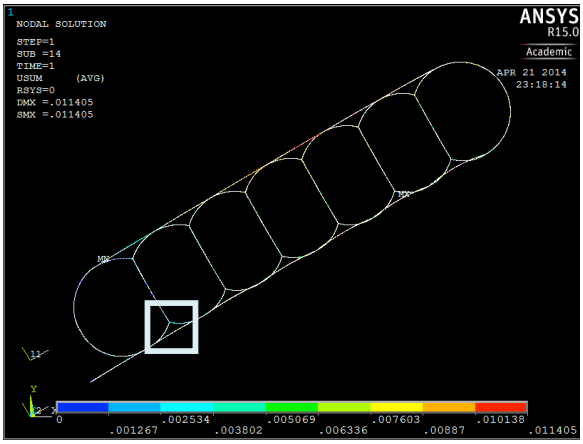

Figure 15. Nonlinear axisymmetric model solution

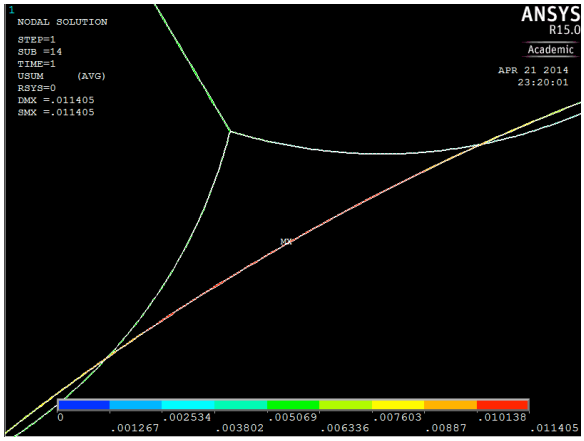

Figure 16. (Inset of fig. 15) Nonlinear solution surface penetration

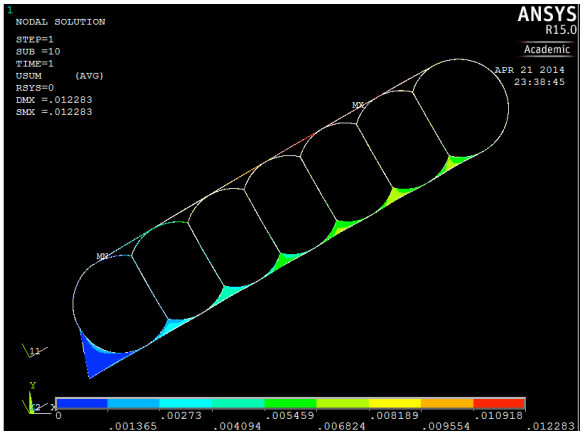

Figure 17. Nonlinear axisymmetric model with filler area solution

Table 3. Results for different models

Model	Linear Geometry Orthotropic Material		Nonlinear Geometry Orthotropic Material		Nonlinear Geometry Isotropic Material	
	Maximum Displacement (m)	Maximum Stress (MPa)	Maximum Displacement (m)	Maximum Stress (MPa)	Maximum Displacement (m)	Maximum Stress (MPa)
15° Wedge Model	0.0929	87.4				
Axisymmetric Model	0.0924	75.6	0.0114	29	0.0168	27.9
Axisymmetric Model, Filler Material			0.0122	31.2		

The results of all runs are shown in Table 3. The results of the linear wedge and axisymmetric models are to within 1% in deflection and 15% in stress. However, the results of the axisymmetric model using linear and nonlinear solutions exhibit over 100% difference in both displacement and stress. Clearly, a nonlinear solver is necessary to capture the large deflections. When comparing the orthotropic and isotropic simulations the stresses are within 4%, but the deflections differ by 47%. The isotropic materials are slightly stiffer which has a drastic effect on the deflection (since this is a thin, flexible structure). The addition of the filler material in the axisymmetric model results in a 7% difference in both stress and deflection. However, the filler material does increase computational complexity since it increases the area required to mesh and solve. The nonlinear axisymmetric model with orthotropic properties provides a good compromise between accuracy and computational efficiency. If higher accuracy is required or computational time is not an issue, the filler area can be added.

G. Mesh Convergence

A mesh convergence analysis was performed to ensure that the solution was converging correctly. This analysis was performed for the axisymmetric model with orthotropic properties, with and without the filler area. This was particularly important for the very small mesh sizes where the model solution became increasingly expensive. Since plane elements were used to model the thin fabric structures, the maximum mesh size was restricted to be on the order of the thickness of the geometry due to constraints on the element aspect ratio. The minimum fabric thickness was approximately $2x10^{-4}$ meters; therefore, the coarsest mesh should be on the order of 10^{-3} meters to ensure a maximum aspect ratio of 10:1. Shown in Table 4, the largest mesh size was chosen to be 10^{-2} meters in order to better view the mesh convergence trends (though the results at these scales may not be trustworthy). The minimum mesh size was chosen based on considerations of the computation time. Since the model without filler area was much less expensive to solve, it allowed for a much smaller mesh size and better understanding of the mesh convergence trends.

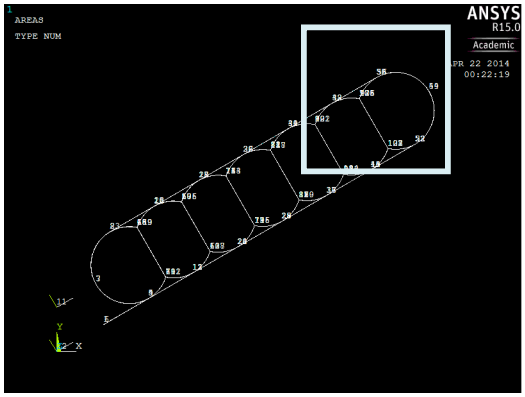

(a) Overall geometry used for mesh convergence

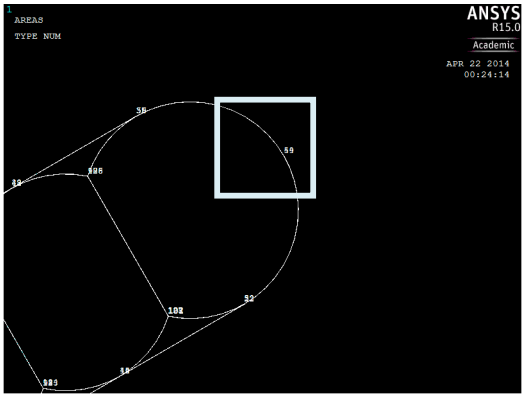

(b) (Inset of a) Zoomed in geometry

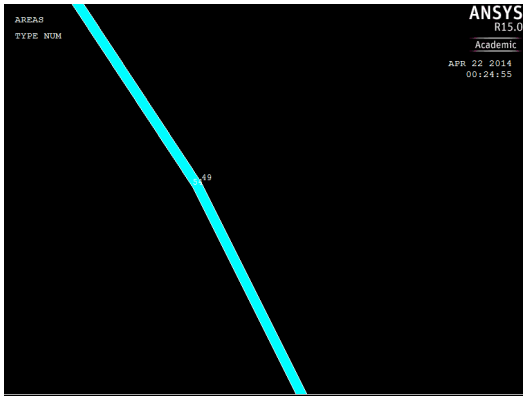

(c) (Inset of b) Zoomed in on keypoint 49

Figure 18. Mesh convergence geometry and location of keypoint 49

The results of the mesh convergence are shown in Table 4. The maximum deflection values stabilize as the mesh size decreases while the maximum stress results diverge. Upon looking into this further it was noticed that the maximum stress values were located at a single node on the aft wrap (see Fig. 24(c) from the Model Validation

section). Therefore, as the mesh size decreased, the result was being divided by a smaller and smaller number, which caused it to diverge. To remedy this problem, the mesh convergence analysis was repeated with the converged stress values being taken at keypoint 49 on the outer tori, seen in Fig. 18, which was subject to a relatively uniform stress field. In this way, the stress values did not artificially diverge and the mesh convergence could be analyzed.

Table 4. Mesh convergence results

Mesh Size	log(Mesh Size)	Maximum Displacement (m)	% Difference in Displacement	Maximum Stress (MPa)	% Difference in Stress
$1x10^{-2}$	-2.0000	0.015209	6.2	26.0	4.1
$7x10^{-3}$	-2.1549	0.014264	7.8	27.1	1.1
$5x10^{-3}$	-2.3010	0.013151	6.5	26.8	0.8
$3x10^{-3}$	-2.5229	0.012291	7.2	26.6	8.3
$1x10^{-3}$	-3.0000	0.011405	0.83	29.0	3.7
$8x10^{-4}$	-3.0969	0.011310	1.3	30.1	6.5
$5x10^{-4}$	-3.3010	0.011163	0.89	32.2	5.8
$3x10^{-4}$	-3.5229	0.011063	0.47	34.2	2.7
$2x10^{-4}$	-3.6990	0.011011	0.49	33.3	21.5
$1x10^{-4}$	-4.0000	0.010957		42.4	

Figures 19 and 20 show the mesh convergence results for maximum displacement and stress at keypoint 49. As seen from Figs. 19, 20 and Table 4, both the maximum displacement and stress results start to converge when the mesh size approaches 10^{-3}. (Convergence here is defined by percent difference less than 5%). This observation confirms the theory on maximum good aspect ratio. When taking into consideration the accuracy and computational cost, the mesh size for the analysis was chosen to be 10^{-3} for all results. This corresponds to the 5^{th} from last point in Figs. 19 and 20.

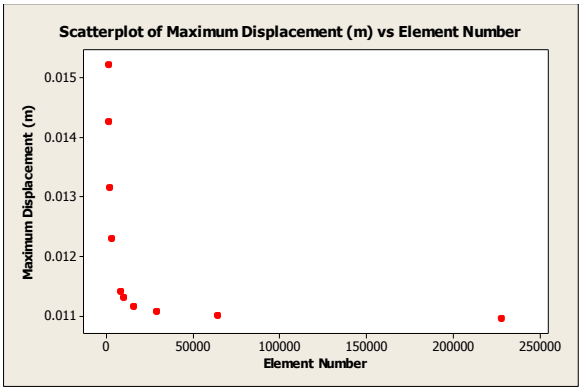

Figure 19. Results from maximum displacement mesh convergence

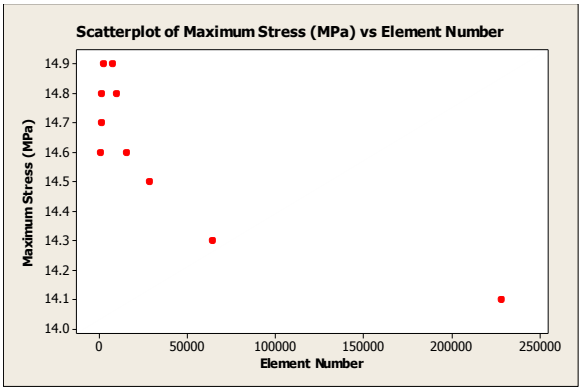

Figure 20. Results from stress mesh convergence performed at keypoint 49

H. Filler Area Convergence

A similar convergence analysis was performed on the elastic modulus of the filler area to ensure that it was not skewing the simulation results by artificially stiffening the structure. For this analysis the elastic modulus of the filler area was successively decreased to see if the maximum deflection and stress stabilized to a given value. Once the analysis converged, the results were extrapolated to an elastic modulus of 0, where the filler material does not provide any stiffness while still preventing surface penetration. Results for stress were taken both at the maximum point and keypoint 49 as in the mesh convergence analysis. These results are shown in Table 5.

Figures 21-23 plot the results of the filler area convergence. Note that convergence goes from right to left in these plots. It is evident from the plots of maximum displacement and stress that as the Young's modulus of the filler area decreases below 10^4, the values start to stabilize. The plot of stress at keypoint 49 shows that there is no effect on the local stress due to the filler material. This proves that the addition of the filler area is a sufficient solution for preventing surface penetration between the tori, spars and forward wrap. The Young's modulus for the

filler area used in this analysis was 1.145 Pa, the lowest value tested in the convergence analysis. This was chosen since the results were well converged by this point and the lower modulus did not significantly hamper computation.

Table 5. Filler material convergence results

Filler Material Young's Modulus (Pa)	Maximum displacement (m)	Maximum Stress (MPa)	Maximum Stress at KP 49 (MPa)
229000	0.010235	28.2	15.2
45800	0.011142	29.8	15.2
22900	0.011569	30.4	15.2
4580	0.012210	31.3	15.2
2290	0.012340	31.3	15.2
458	0.012483	31.3	15.2
229	0.012500	31.3	15.2
45.8	0.012481	31.4	15.2
22.9	0.012465	31.5	15.2
4.58	0.012424	31.5	15.2
2.29	0.012377	31.4	15.2
1.145	0.012283	31.2	15.2

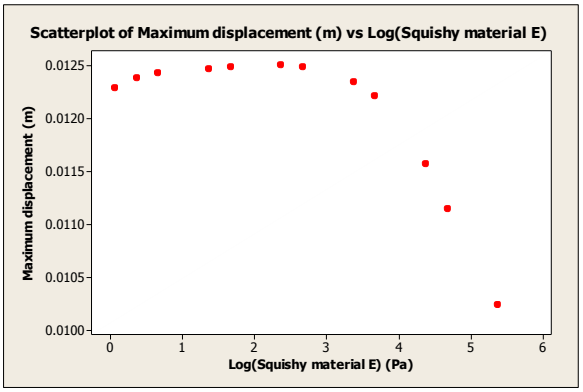

Figure 21. Maximum displacement during filler area convergence

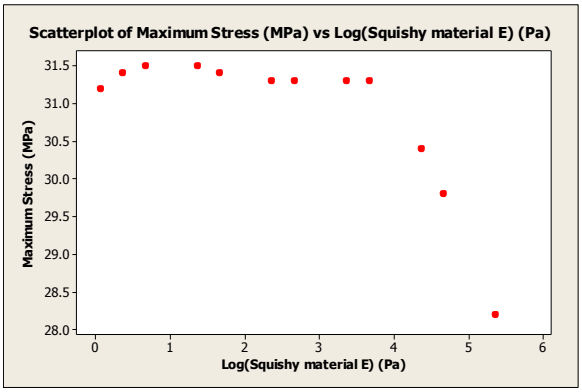

Figure 22. Maximum stress during filler area convergence

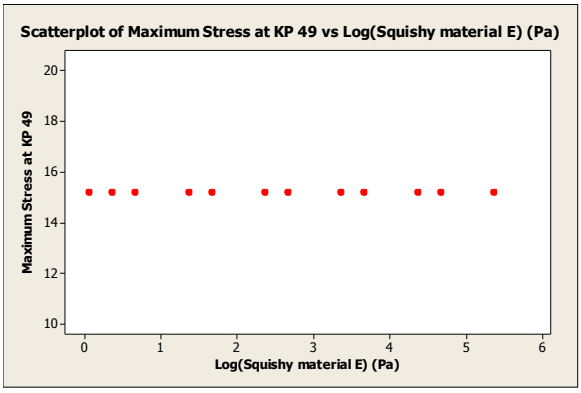

Figure 23. Stress at keypoint 49 during filler area convergence

IV. Model Validation

Closed-form solutions are available to calculate the stress in the tori, spars and restraint wrap for simplified geometries, shown in Eqs. 1-3 respectively.[3] The values used for each variable are shown in Table 6. The FEA model developed in this report was validated against the closed-form equations and the literature, seen in Table 7.[3]

$$N_{MAX} = \frac{PD_T}{4}\left(2 + \frac{D_T}{D_C}\right) \tag{1}$$

$$N_{MAX} = \frac{PW_S}{2}\left(1 + \frac{1}{1 - \frac{H_S \cos(\alpha)}{D_C + D_T + W_S \sin(\alpha)}}\right) \approx PW_S \tag{2}$$

$$N_{MAX} = \frac{m_C a}{2\pi D_C \cos(\alpha)} \tag{3}$$

Table 6: Variables use in equations 1-3

P (psi)	D_T (m)	D_C (m)	W_S (m)	α (deg)	H_S (m)	m_c (lb)	a (m/s^2)
3.0	0.305	0.376	0.204	60	0.227	150	7.7g

Table 7 confirms that the finite element solution matches both the closed-form equations and the literature results to within approximately 5%. The only exception is with the stresses in the aft section of the wrap. However, as was noted in the mesh convergence section, this was due to a singularity where the wrap had clamped boundary conditions and was attached to a torus (seen in Fig. 24(c)). Therefore, the wrap aft stress value is dependent on the mesh size and is not physical.

Table 7: Finite element results vs. closed-form solutions and literature results

Fabric Location	Finite Element Results (lb/in)	Literature Results (lb/in)	Closed-form Equation (lb/in)	% Difference
Tori	26.5	28.4	27.9	-4.9
Spar	27.6	26.8	26.1	5.6
Wrap Fwd	25.5	22.0	24.8	2.9
Wrap Aft	45.3	28.7	24.8	82.5

The location of the maximum stress values match those predicted by the closed form equations and presented in the literature. These locations can be seen in Fig. 24. The maximum stress value for the tori lay on the inner radius of the inner torus and the maximum forward and aft wrap stresses occurred at their attachment to the center-body. The one exception is the location of the spar maximum stress. The literature results found the maximum spar stress to be on the inner spar at its intersection with tori on the forward side. However, since the stress values between the different spars did not vary significantly, this discrepancy is not of consequence.

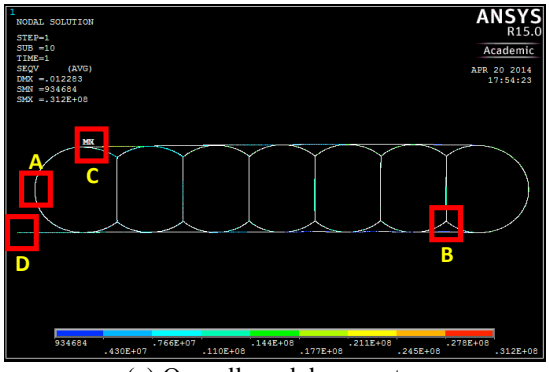

(a) Overall model geometry

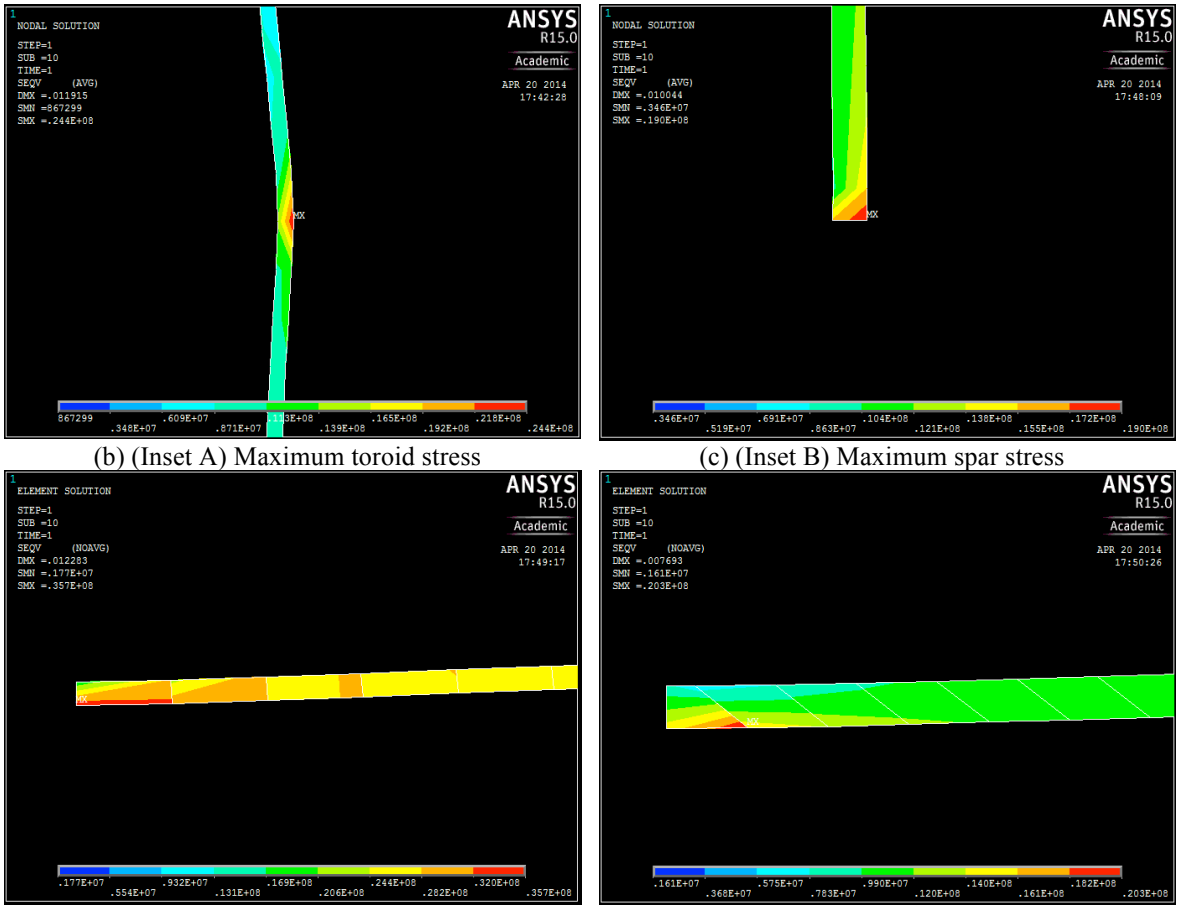

(b) (Inset A) Maximum toroid stress

(c) (Inset B) Maximum spar stress

(d) (Inset C) Maximum aft wrap stress

(e) (Inset D) Maximum forward wrap stress

Figure 24. Maximum stress results for all components of the axisymmetric model

V. Conclusion

In this investigation, a finite element model of a hypersonic inflatable aerodynamic decelerator (HIAD) was created. The geometry of the HIAD includes seven inflatable tori separated into three inflatable volumes. Tori are sectioned by spars and held together by a restraint wrap. Two structural models were created: a 3D, 15° wedge model and a 2D, axisymmetric plane model, both exploiting the symmetry of the problem. Results were calculated for both orthotropic and isotropic material properties. An additional model was created that included an artificial 'filler' area in between the tori and forward restraint wrap. This low elastic modulus material prevented contact with minimal stiffening of the structure. The models were subject to a 3 psi inflation pressure acting outwards on all of the tori as well as an aerodynamic pressure of 0.22 psi acting on the surface of the forward restraint wrap. Symmetric boundary conditions were applied to the symmetry planes, roller boundary conditions were applied to the intersection of the inner tori and the center-body and the forward and aft restraint wraps were clamped at the center-body.

Results obtained from the linear finite element solver showed significant surface penetration and unrealistic results. Results obtained using isotropic material properties had similar stress values but significantly different deflections. Results obtained with and without the addition of filler areas were in agreement to 7%. Therefore, it is suggested to use the model without filler area for faster results.

A mesh convergence analysis was performed. Maximum mesh size was limited by poor aspect ratio elements. However, the results converged for element size of 10^{-3}, which correlated well with theory on maximum good aspect ratio. An additional convergence analysis was performed for the Young's modulus of the filler material. It was determined that the filler material had minimal effect for reasonable values of Young's modulus.

The model was validated with closed-form equations and literature results. All stress values correlated well except for the maximum stress on the aft restraint wrap due to a singularity. In addition, the locations of the maximum stresses correlated well.

Acknowledgments

Many thanks to Michael Lindell and Crystal Fenn of the NASA Langley Research Center for their help with the material properties and Wei Chen of Georgia Institute of Technology for his support on the model convergence. This project was completed during the tenure of the National Science Foundation Graduate Research Fellowship Grant #DGE-1148903 and NASA Science and Technology Research Fellowship Grant #NNX12AM33H.

References

[1] Hansen, James R. (Jun 1987). "Chapter 12: Hypersonics and the Transition to Space". Engineer in Charge: A History of the Langley Aeronautical Laboratory, 1917-1958. The NASA History Series. sp-4305. United States Government Printing. ISBN 978-0-318-23455-7.

[2] NASA Launches New Technology: An Inflatable Heat Shield, NASA Mission News, 2009-08-17, accessed 2011-01-02.

[3] M. C. Lindell, S. J. Hughes, M. Dixon, and C. E. Willey, "Structural Analysis and Testing of the Inflatable Re entry Vehicle Experiment (IRVE)," AIAA Paper AIAA 2006-1699, 47th AIAA/ASME/ASCE/AHS/ASC Structures, Structural Dynamics, and Materials Conference, Newport, Rhode Island, May 1-4 2006.